Ramjets: Thermal Management – An Integrated Engineering Approach

Ronald G. Veraar
TNO Defence, Security and Safety
P.O. Box 45
2280 AA Rijswijk
NETHERLANDS

ronald.veraar@tno.nl

ABSTRACT

Within the framework of the VKI/RTO Lecture Series on 'High Speed Propulsion: Engine Design – Integration and Thermal Management', this lecture focuses on thermal management of ramjet propulsion systems. This is done by describing an engineering model that can be used to perform an integrated thermal analysis of a supersonic/hypersonic ramjet propelled vehicle in conjunction with an integrated performance evaluation of the aerodynamic and propulsive performance of the vehicle. The thermal analysis considers the combined thermal loading from aerodynamic heating on the outer surfaces of the vehicle and from internal reactive gas dynamic heating inside the propulsion system. Especially for highly integrated high-speed airbreating propelled vehicles the resulting tool is very valuable to support the vehicle design process in its early stage.

1.0 INTRODUCTION

Looking at weapon systems under development, there is a clear trend towards longer range and higher flight speeds. At the same time, for civil applications, there is a need to reduce the propellant mass fraction to enable more affordable access to space. For both applications, high speed airbreathing propulsion can be considered an important enabling technology.

A subsonic combustion ramjet combines mechanical simplicity with high propulsive efficiency. Its operational Mach number range of 2 to 6 or 7 makes this propulsion system especially attractive for air launched or gun launched applications. However, at flight Mach number of 4 and higher, the aerodynamic heating of external surfaces becomes significant. The compression process in the intake to subsonic flow velocity results in very high temperatures of the gasses in the internal flow path inducing excessive heat loads on the combustor and nozzle walls. At the same time, the high temperatures result in substantial dissociation losses which reduce the propulsive efficiency at the high Mach number end of the operational regime of the ramjet.

This poses the designer of ramjet propulsion systems with several challenges. First of all, the heat loads need to be known. And secondly, ways need to be found how to handle these heat loads in terms of choice of materials, application of thermal protection and passive or active cooling. This drives the need for a thermal analysis of the integrated vehicle early in its design stage.

The present lecture describes a thermal model as part of the integrated engineering system model HyTEC. This engineering model covering integrated aerodynamic and propulsive performance is extended with an integrated thermal model capable of predicting the combined aerodynamic and reactive gas dynamic thermal loads on complex ramjet propelled vehicles.

2.0 AERODYNAMIC HEATING

2.1 General Heat Transfer Relations

The air flow around any vehicle moving through the atmosphere comes to rest at the stagnation point and adjacent to the wall in the boundary layer. At these points the kinetic energy of the flow is converted into thermal energy, resulting in a convective heat flux from the air flow to the structure of the vehicle. The basic equation describing convective heat transfer is:

$$q_c = h_c\,(T_{aw} - T_w) \tag{2.1}$$

in which q_c is the convective heat flux to the wall, h_c is the convective heat transfer coefficient, T_{aw} is the adiabatic wall temperature and T_w is the wall temperature. The adiabatic wall temperature T_{aw} is the equilibrium wall temperature of a thermally isolated wall (i.e. no heat addition or cooling). From Eq. (2.1) it can be seen that if the wall temperature is equal to the adiabatic wall temperature, the heat flux becomes zero and no heat is added to or extracted from the air flow. The convective heat transfer coefficient is dependent on the fluid properties and can be described by several dimensionless numbers which will be defined below. The heat flux of a caloric perfect gas parallel to the wall is given by:

$$q = \rho\, v\, c_p (T_{aw} - T_w) \tag{2.2}$$

in which ρ is the density, v is the velocity and c_p is the specific heat at constant pressure of the gas. The Stanton number is defined as the ratio of the heat flux normal to the wall (Eq. (2.1)) to the heat flux parallel to the wall (Eq. (2.2)):

$$St = \frac{h_c}{\rho\, v\, c_p} \tag{2.3}$$

The relative importance of viscosity and conductivity in a fluid is expressed by the Prandtl number:

$$Pr = \frac{c_p\ \mu}{k} \tag{2.4}$$

in which μ is the dynamic viscosity and k is the conductivity of the fluid. The relative importance of inertial forces with respect to viscous forces is given by the Reynolds number:

$$Re = \frac{\rho\, v\, L}{\mu} \tag{2.5}$$

where L is a suitable chosen reference length. Finally, the relative importance of convective and conductive heat transfer is expressed by the Nusselt number:

$$Nu = \frac{h_c\ L}{k} = St\ Re\ Pr \tag{2.6}$$

Using Eq. (2.3), the convective heat flux from a caloric perfect gas to the wall follows from:

$$q_c = St\ \rho\ v\ c_p(T_{aw} - T_w) \tag{2.7}$$

To take into account the imperfect caloric behaviour of air ($c_p \neq$ constant) at the high static temperatures involved in the boundary layer at supersonic and hypersonic flight speeds the heat flux to the wall needs to be expressed in terms of an enthalpy difference instead of a temperature difference. With the enthalpy defined as:

$$h = \int c_p\ dT \tag{2.8}$$

Eq. (2.7) can be rewritten to:

$$q_c = St\ \rho\ v\ (h_{aw} - h_w) \tag{2.9}$$

The adiabatic wall enthalpy h_{aw} is defined as:

$$h_{aw} = h + r\frac{v^2}{2} \tag{2.10}$$

in which r is the so called recovery factor which follows from:

$$r = Pr^a \tag{2.11}$$

with a = ½ for a laminar boundary layer and a = ⅓ for a turbulent boundary layer.

2.2 Reynolds Analogy

The Reynolds analogy results in the following relation between the convective heat transfer and the friction coefficient c_f:

$$St = \frac{c_f}{2\,Pr^{2/3}} \tag{2.12}$$

The friction coefficient for a compressible boundary layer on a flat plate in absence of leading edge disturbances and viscous interaction follows from:

$$c_f = \frac{0.664}{\sqrt{Re_x}\left(\frac{T'}{T_\infty}\right)^{\frac{1-\omega}{2}}} \tag{2.13}$$

for a laminar boundary layer and

$$c_f = \frac{0.0592}{Re_x^{1/5}\left(\frac{T'}{T_\infty}\right)^{\frac{4-\omega}{5}}} \tag{2.14}$$

for a turbulent boundary layer, in which ω is the exponent describing the relation between the viscosity and the temperature which is used to account for the correct value of the viscosity at a representative value of the temperature within the boundary layer, the so-called reference temperature T'. For an isothermal wall (T_w = constant) this reference temperature follows from:

$$\frac{T'}{T_\infty} = 1 + 0.032 M_\infty^2 + 0.58\left(\frac{T_w}{T_\infty} - 1\right) \tag{2.15}$$

for a laminar boundary layer, and

$$\frac{T'}{T_\infty} = 1 + 0.035 M_\infty^2 + 0.45\left(\frac{T_w}{T_\infty} - 1\right) \tag{2.16}$$

for a turbulent boundary layer. Combining Eq. (2.12) through Eq. (2.14) and using $\omega = 0.76$ and $Pr = 0.71$ (both are representative values for air over a relatively broad range of air temperatures), the convective boundary layer heat transfer on a flat plate is given by:

$$St = \frac{0.417}{\sqrt{Re_x}\left(\frac{T'}{T_\infty}\right)^{0.12}} \tag{2.17}$$

for a laminar boundary layer and

$$St = \frac{0.0317}{Re_x^{1/5}\left(\frac{T'}{T_\infty}\right)^{0.648}} \tag{2.18}$$

for a turbulent boundary layer.

2.2 Aerodynamic Heating of a Flat Plate

Figure 1 shows the components of the aerodynamic heating model of a flat plate using the Reynolds analogy equations described in the previous section. Given the flight altitude, the static atmospheric temperature, pressure and density can be derived from the equations describing the standard atmosphere (e.g. [1]). The evaluation of the aerodynamic heating requires several gas properties of air to be known. Assuming the air to be a thermally (but calorically imperfect) gas, the ratio of specific heats can be calculated from [2]. In addition, to correctly account for the calorically imperfect behaviour of air and the temperature dependency of the viscosity in the inviscid flow field, polynomials are used based on data obtained from chemical equilibrium calculation using CEA2000 [3]. To describe the change of conditions across the shock wave, the caloric imperfect oblique shock wave relations of [2] are used.

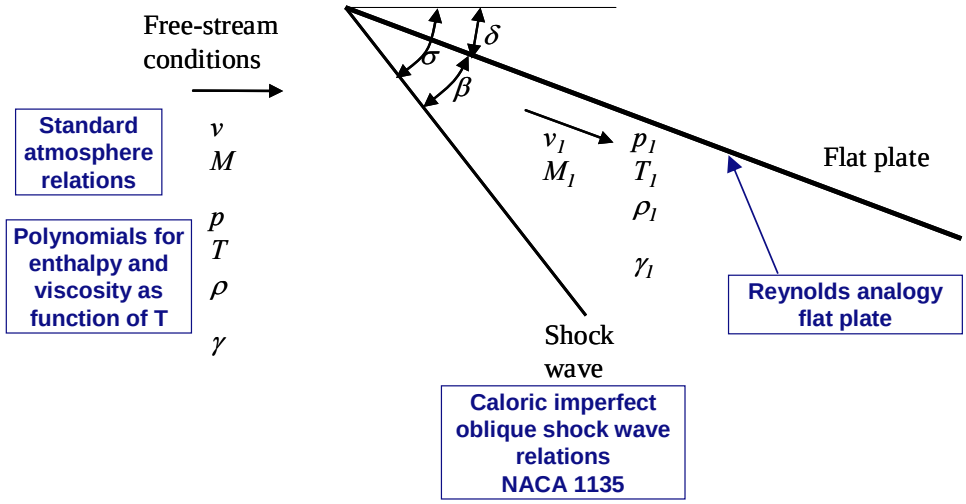

Figure 1: Aerodynamic heating model description of a flat plate at angle of attack.

Figure 2 shows the predicted level of Stanton number and heat flux for a flat plate at an angle of attack from 0 to 15 degrees for a laminar and turbulent boundary layer. As can be seen the turbulent Stanton number is significantly higher than the laminar boundary layer. The figure clearly shows the resulting heat flux levels to increase at increasing angle of attack.

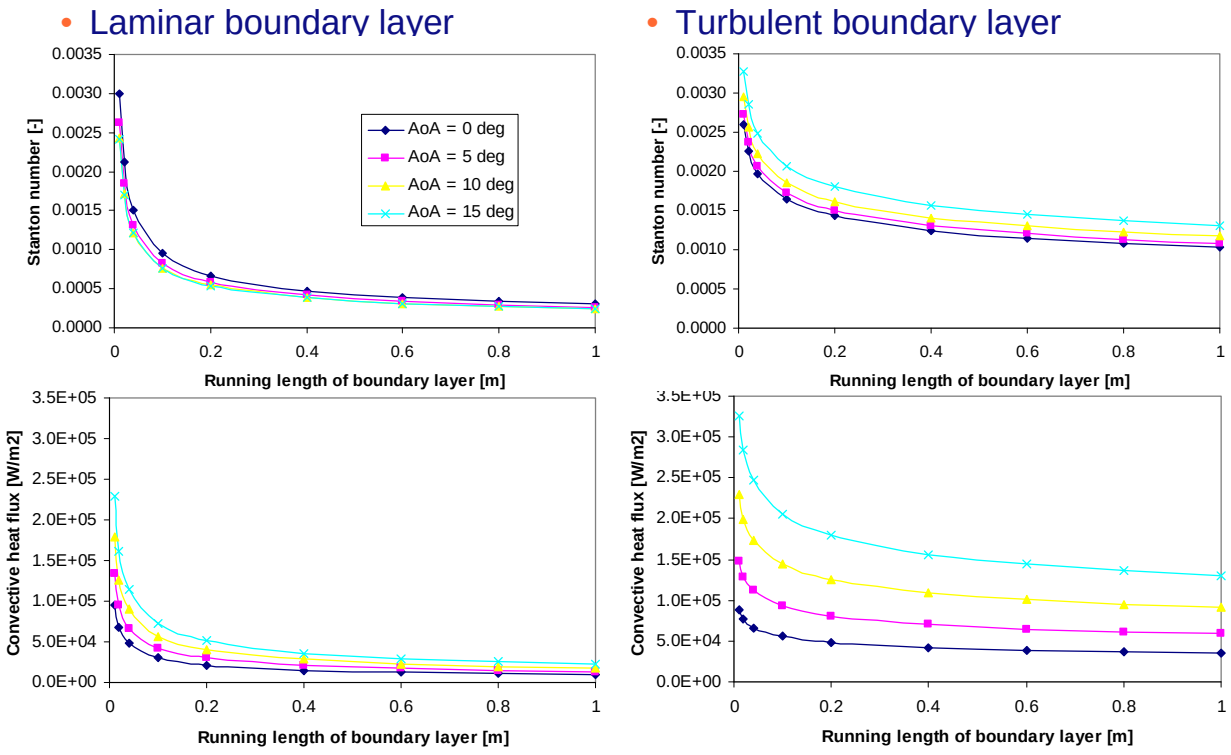

Figure 2: Predicted Stanton number (top) and heat flux (bottom) for laminar (left) and turbulent boundary layer (right) on a flat plate at angle of attack at Mach 6 and 32 km altitude.

2.3 Aerodynamic Heating of Convex Surfaces

Figure 3 shows the aerodynamic heating model components for two convex flat surfaces. In between the two flat plates the supersonic flow expands. This isentropic expansion is described using the well-known Prandtl-Meyer relations [2].

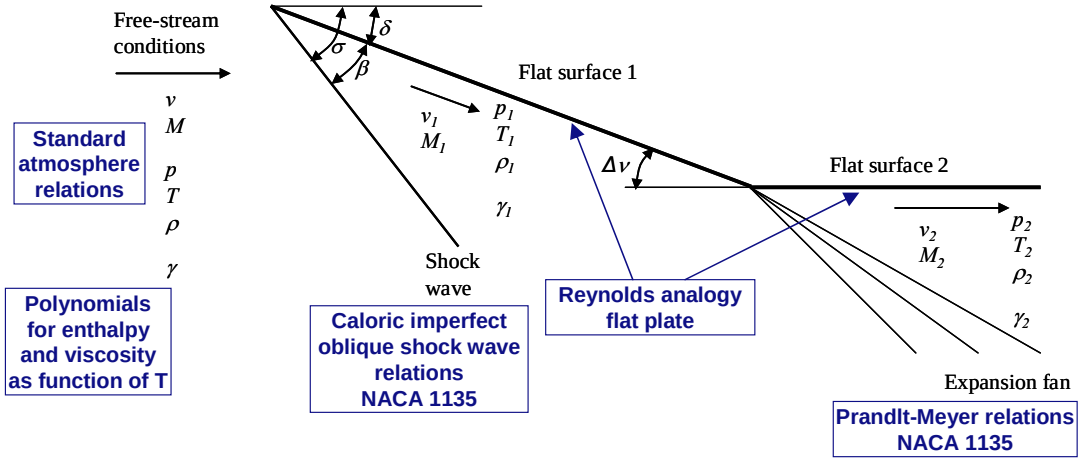

Figure 3: Aerodynamic heating model description of two flat convex surfaces.

Figure 4 shows a typical predicted heat flux level for two convex surfaces. For this example case, both surfaces have a length of 1m and the expansion angle $\Delta\nu$ is 15 degrees. The vehicle is assumed to fly at Mach 6 at an altitude of 32 km with a local inclination angle of the first surface of 15 degrees and wall temperatures of 1000 K. The boundary layer is assumed to be laminar. The expansion of the flow clearly results in a reduction of the heat load on the second surface.

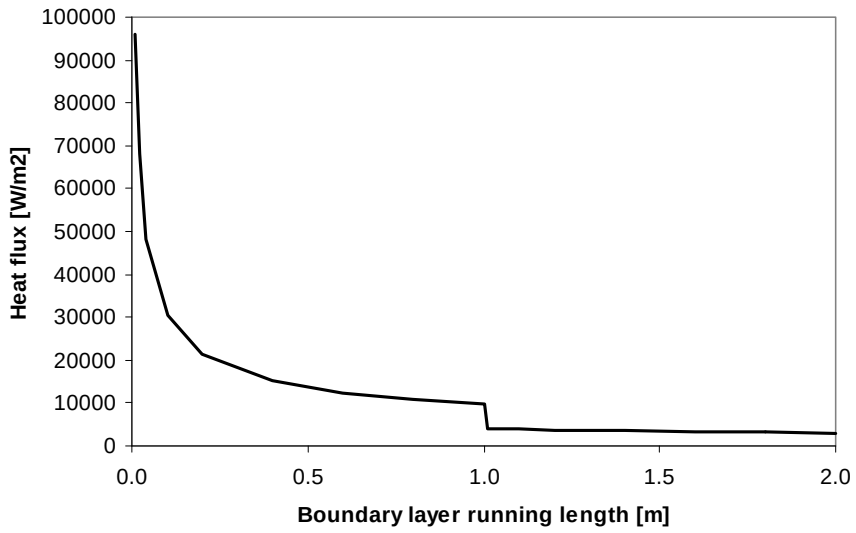

Figure 4: Example of predicted heat flux level on two convex flat surfaces at Mach 6 and 32 km altitude assuming a laminar boundary layer.

2.4 Aerodynamic Heating of a Cone

Figure 5 shows the components of the aerodynamic heating model of a cone. In contrast the supersonic flow across a flat plate at angle of attack, where the flow conditions downstream of the shock wave remain constant, a method is now required to calculate the flow conditions at the cone surface from the conditions downstream of the shock wave. This may be done by using the well-known Taylor-Maccoll relations which require numerical solution. As an alternative, in the present model the analytical relations of [4] are used. In addition, a correction factor of 1.15 [5] is applied to account for the higher level of Stanton number on a cone when compared to a flat plate at the same local inviscid flow conditions.

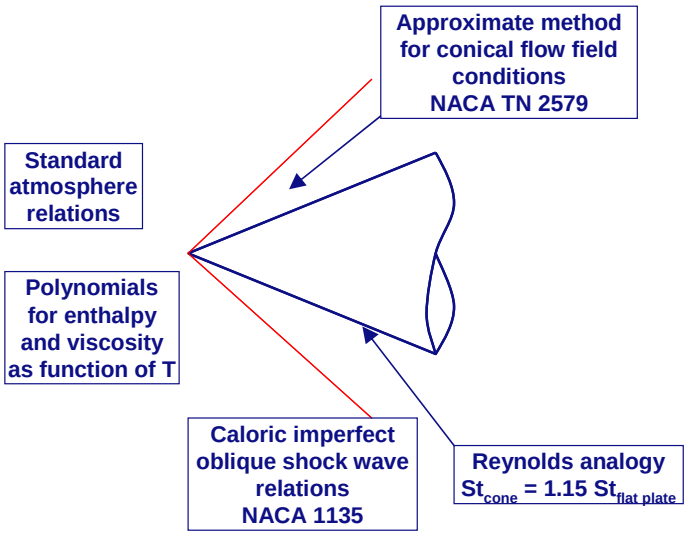

Figure 5: Aerodynamic heating model description of a cone.

From Eq.(2.7) it follows that the wall temperature will increase until the wall temperature becomes equal to the adiabatic wall temperature. At higher wall temperatures radiation of heat from the wall to the surroundings will become significant. This radiating heat component will result in a so-called thermal equilibrium wall temperature well below the adiabatic wall temperature. The radiative heat transfer can be evaluated from:

$$q_{rad} = \varepsilon \sigma T_w^4 \tag{2.19}$$

with ε being the emissivity (assumed value of 0.8) and σ being the Stefan-Boltzman constant ($5.6704 \cdot 10^{-8}$ W/m^2K^4). Neglecting conduction of heat in the wall parallel to the wall surface, the thermal equilibrium wall temperature as a function of length along the cone surface follows from iterating the wall temperature at each position along the surface until the local convective heat flux equals the local radiative heat flux.

To illustrate the effectiveness of radiation cooling the thermal equilibrium wall temperatures have been predicted using the aerodynamic heating model of a cone assuming Mach 6 free stream conditions at 32 km altitude and assuming a turbulent boundary layer. Figure 6 shows the adiabatic wall temperature and the thermal equilibrium wall temperatures for values of the emissivity from 0.2 to 0.8. As can be seen radiative cooling can be rather efficient.

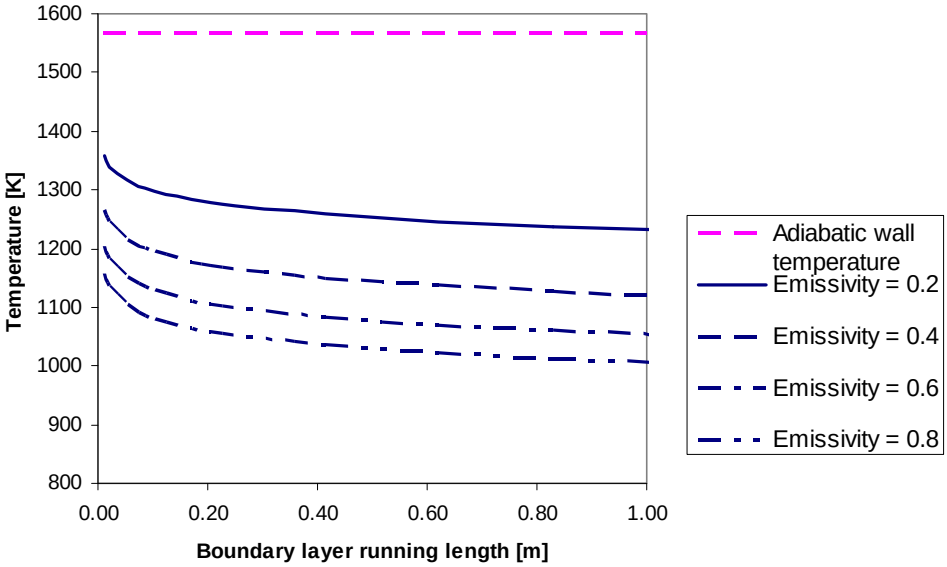

Figure 6: Predicted thermal equilibrium wall temperatures for a turbulent boundary layer on a cone at Mach 6 and 32 km altitude.

2.5 Application Case: Aerodynamic Heating of a Cone-Cylinder-Flare

To verify the aerodynamic heating model, free flight data of a cone-cylinder-flare configuration is used from [6]. The flight tests performed were part of a research program to investigate high-speed aerodynamic heat transfer. Instrumented models were launched by rocket motors to measure rates of skin heating at hypersonic speeds. The model used in this particular flight test is shown in Figure 7. The model was made of Inconel and had a wall thickness of 0.03 inch. 23 thermocouples were spotwelded to the inner skin surface of the model. Accelerometers were installed to measure the thrust, drag, normal and transverse accelerations.

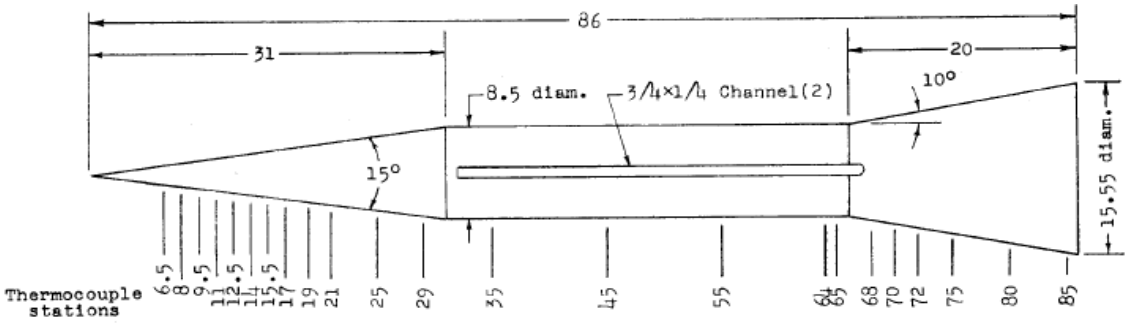

Figure 7: Model dimensions and thermocouple stations (dimensions in inches).

The flight testing was carried out using a 4 stage rocket motor propulsion system, launched at a 70 degrees elevation angle. Figure 8 shows the complete flight test vehicle at its launch site. During flight, telemetry was used to retrieve the thermocouple and accelerometer data from the model. A Doppler radar was used for vehicle tracking. During this particular flight test the 4th stage did not ignite, resulting in a maximum Mach number of 4.7 instead of 9.

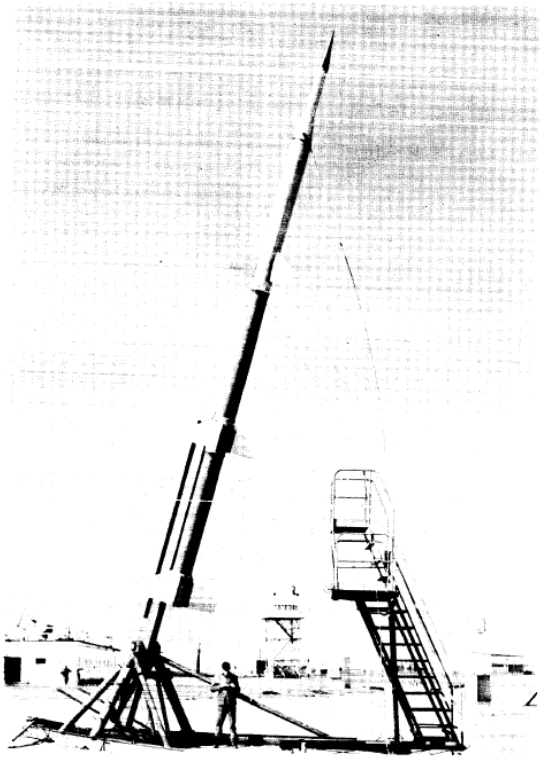

Figure 8: Model and boosters on launch site.

An example of typical temperature data that was acquired is shown in Figure 9. From these temperature profiles, the local Stanton numbers were derived taking into account both external and internal radiation.

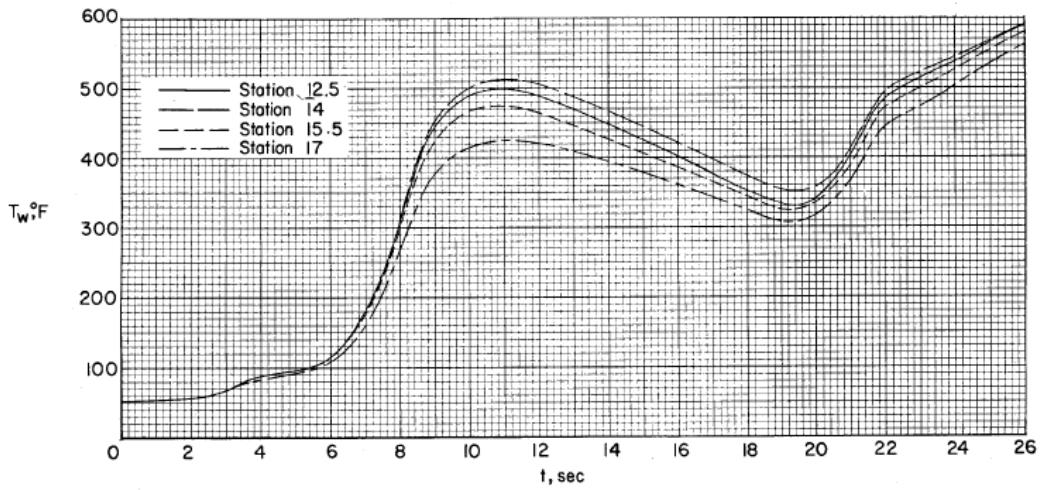

(b) Nose-cone stations 12.5, 14.0, 15.5, and 17.0.

Figure 9: Example of wall temperatures measured in flight.

Figure 10 shows the components of the aerodynamic heating model used. The Stanton multiplication factor of 1.15 is applied both at the nose cone and on the flare surface.

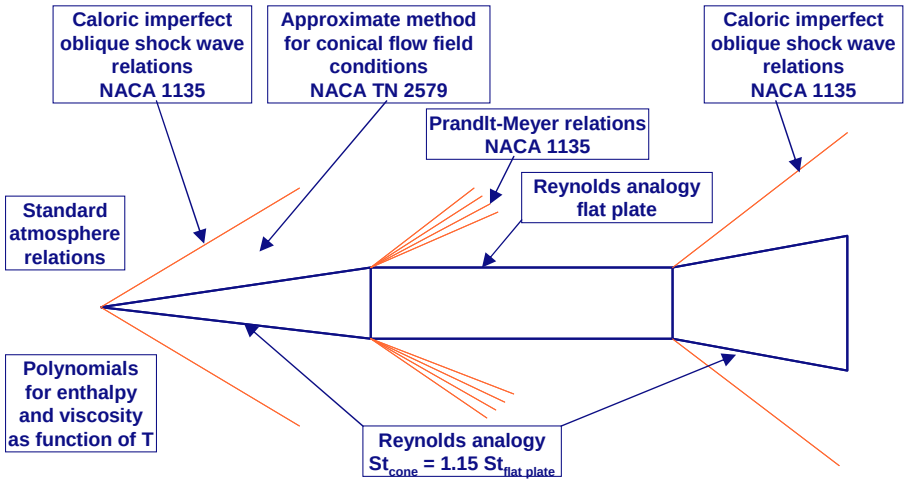

Figure 10: Aerodynamic heating model description of a cone-cylinder-flare.

Figure 11 shows the local Stanton numbers derived from the flight data compared with the predicted Stanton numbers assuming the boundary layer to be turbulent. As can be seen the general agreement is quite good. At the nose cone, the experimental data shows evidence of boundary layer transition from laminar to turbulent. The predicted changes of Stanton number level both at the cone-cylinder and at the cylinder-flare interface are close to those derived from the flight model. On the flare surface, the flight test data show an increasing Stanton number which is not captured by the aerodynamic heating model. Conical flow field effects of the flow around the flare are not accounted for the present version of the model.

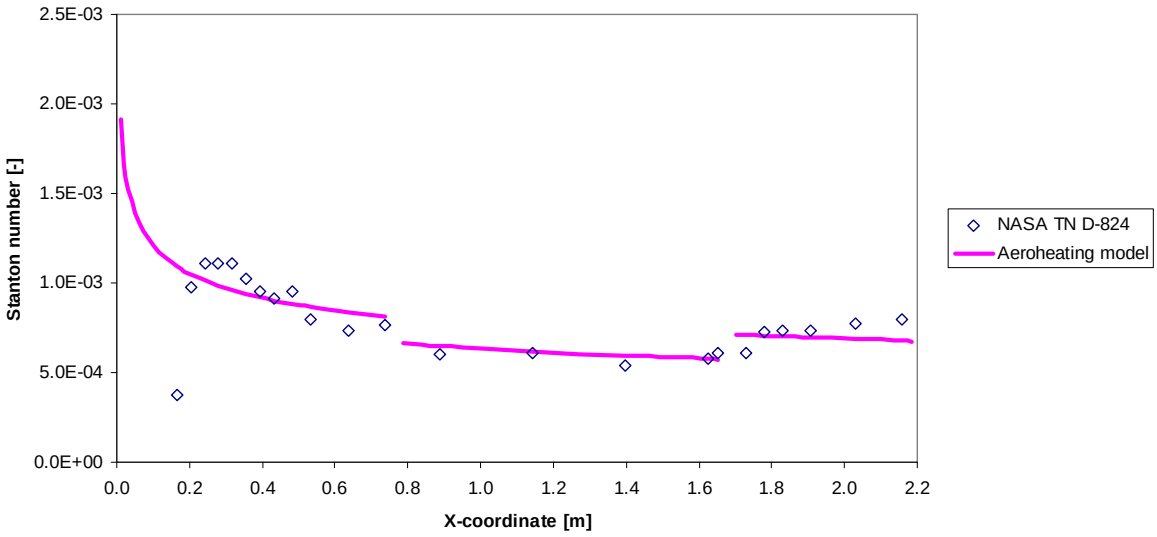

Figure 11: Comparison of aerodynamic heating model results with free flight data.

3.0 RAMJET INTERNAL GAS DYNAMIC HEATING

The model to predict the internal gas dynamic heating of the ramjet propulsion system will be treated in two separate parts: 1) the internal intake duct (Section 3.1) where there is only air flowing through the system, and 2) the combustor and nozzle (Section 3.2) where fuel is injected, mixed and burned with the

air and finally expanded to generate thrust. Figure 12 shows a schematic representation of the ramjet propulsion system to indicate the general layout of the propulsion system.

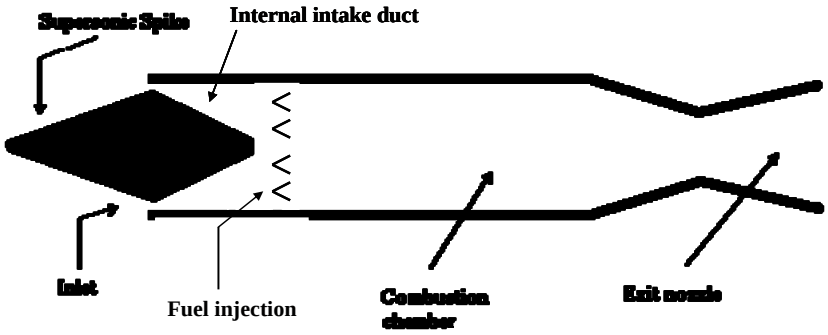

Figure 12: Schematic representation of the ramjet propulsion system.

3.1 Internal Intake Duct

The internal intake configuration is an annular duct defined by the inner contour of the intake cowl and the outer contour of the intake centre body. For the internal heating of the intake subsystem of the propulsion system (i.e. the subsonic diffuser) the Colburn relation for heat transfer in fully developed turbulent pipe flows is adopted:

$$St = 0.023\,\mathrm{Re}_D^{-0.2}\,\mathrm{Pr}^{-0.67} = 0.023\left(\frac{\rho v D}{\mu}\right)^{-0.2}\mathrm{Pr}^{-0.67} = 0.023\left(GD_H\right)^{-0.2}\mu^{0.2}\,\mathrm{Pr}^{-0.67} \qquad (3.1)$$

In this relation, the gas properties μ and Pr are to be evaluated at a temperature representative for the mean conditions in the boundary layer (i.e. the film temperature).

Equation (3.1) is especially convenient because the gas properties term $\mu^{0.2}\mathrm{Pr}^{-0.67}$ is approximately constant as a function of the temperature. Due to this feature, a single representative value for this term can be used to calculate the Stanton number throughout the subsonic diffuser. This is illustrated in Figure 13 which shows the value of the transport properties of air as a function of the range of total temperatures to be expected in the ramjet intake duct. The specific heat at constant pressure, conductivity and the viscosity all show significant dependence on the temperature. The term $\mu^{0.2}\mathrm{Pr}^{-0.67}$, however, remains practically constant, allowing for one representative value to be selected for and used in the internal intake duct heating model.

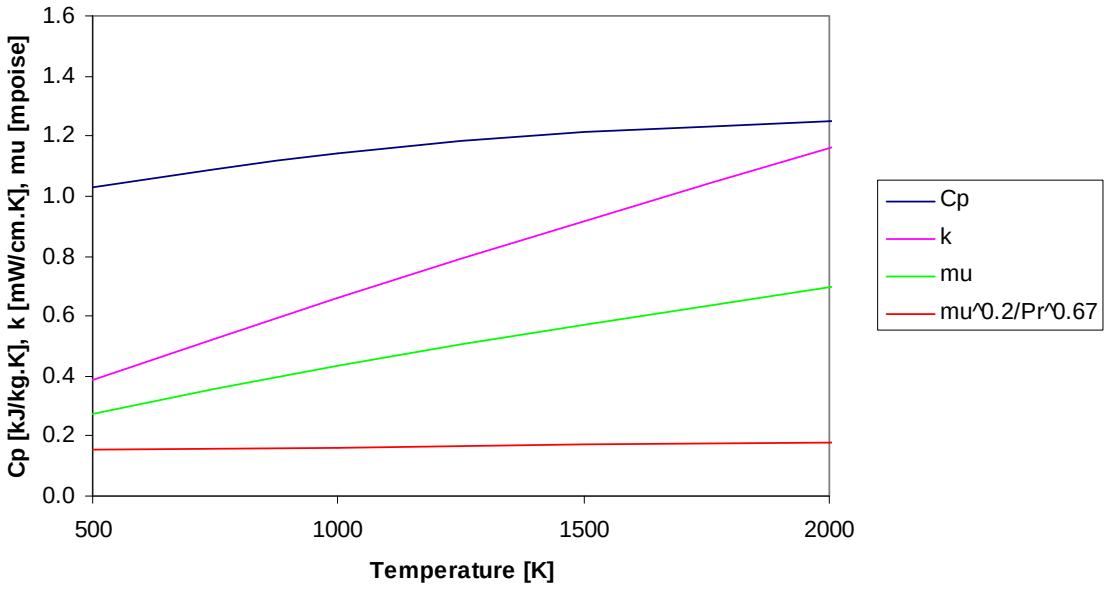

Figure 13: Transport properties of air as calculated using CEA2000 [3].

In the thermal model the internal flow conditions are calculated such that the mass and energy of the air flow is conserved. This is done using the flow relations for a thermally perfect but calorically imperfect gas from [2].

To also include the effect of radiation of heat the model is extended by an internal radiation heat flow term for co-axial cylinders [6]:

$$q_{radi,x} = \frac{\sigma\left(T_{cowl,x}^4 - T_{CB,x}^4\right)}{\left(\frac{r_{cowl,x}}{r_{CB,x}}\frac{1}{\varepsilon_{CB}} + \frac{1}{\varepsilon_{cowl}} - 1\right)} \tag{3.2}$$

Depending on which wall temperature is higher (the temperature of the cowl ($T_{cowl,x}$) or the temperature of the intake center body ($T_{CB,x}$)), this radiative heat flow should be added to or subtracted from the heat input to the inner and outer wall of the intake duct. In this analysis it is assumed that the intake cowl wall thickness is infinitely small and assuming the internal and external intake cowl wall temperature to be equal.

3.2 Combustor and Nozzle

The combustor of the generic ramjet propulsion system shown in Figure 12 is essentially a cylindrical duct. The internal nozzle contour can also be treated as a cylindrical duct with varying diameter. As for the internal intake duct, the walls of the combustor and nozzle are assumed to be infinitely thin and the internal and external wall temperatures are assumed to be equal. The convective heat load can be evaluated in a similar manner as for the internal intake duct described in the previous section.

In order to select a representative value of the $\mu^{0.2}Pr^{-0.67}$ term for the combustion products in Equation (3.1), the values of specific heat at constant pressure, conductivity and viscosity have been calculated using the chemical equilibrium code CEA2000 [3]. The fuel is assumed to be Jet-A and Figure 14 shows

the results of the CEA2000 calculations of pure air and that of air/fuel mixture having equivalence ratios of 0.4 up to 1 (i.e. the stoichiometric mixture ratio). Increasing the mixture ratio results in higher values of the specific heat at constant pressure and of the conductivity. The viscosity is hardly affected by the equivalence ratio. As can be seen, the value of the $\mu^{0.2}Pr^{-0.67}$ term again remains practically constant throughout the range of equivalence ratios and gas temperatures considered to be representative for the ramjet propulsion system.

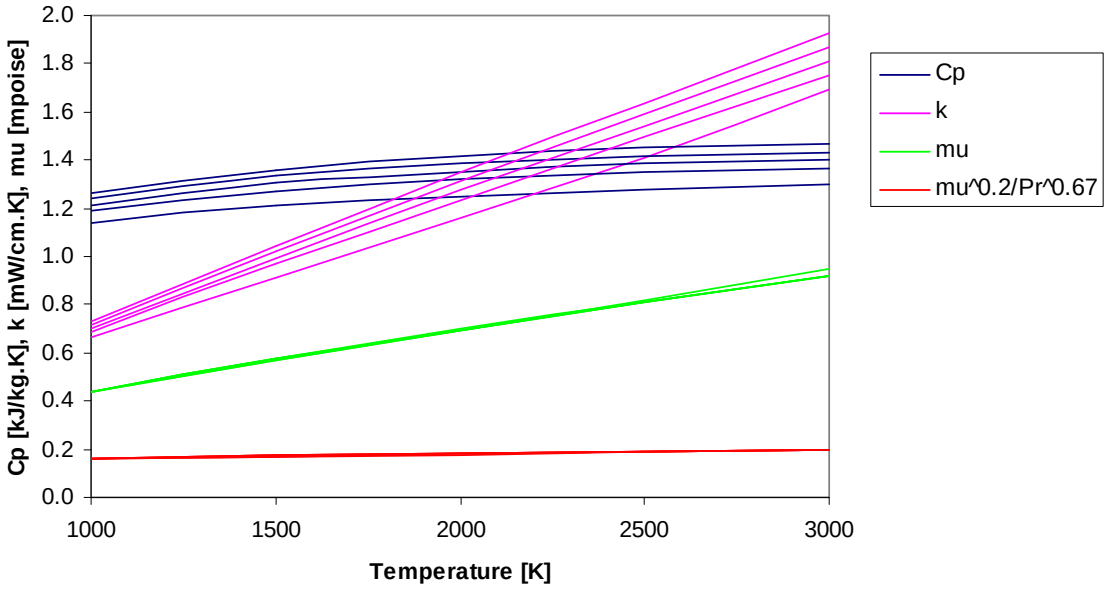

Figure 14: Transport properties of air/Jet-A mixtures with equivalence ratio of 0 to 1 as calculated using CEA2000 [3].

Throughout the combustor and nozzle the internal flow conditions are calculated such that the mass and energy of the flow is conserved. This is done using the flow relations for a thermally perfect but calorically imperfect gas from [2].

4.0 INTEGRATED THERMAL MODEL OF SHYFE RAMJET VEHICLE

As an application case study of the developed thermal model, the SHyFE vehicle has been modelled in HyTEC and both the aerodynamic and propulsion module as well as the thermal module were used to evaluate the integrated performance of the SHyFE vehicle.

The Sustained Hypersonic Flight Experiment (SHyFE) was initiated by QinetiQ around the year 2000 [7]. The UK Ministry of Defence funded program aimed to design, manufacture and flight test a small demonstrator of a hypersonic cruise vehicle. The SHyFE vehicle (see Figure 15) was to be launched by a rocket booster to Mach 4 at an altitude of 15 km. After booster separation the flight demonstrator was intended to accelerate and climb under its own power to Mach 6 at 32 km altitude. At the latter flight conditions the vehicle would cruise for about 300 km prior to fuel burn-out and an uncontrolled descent.

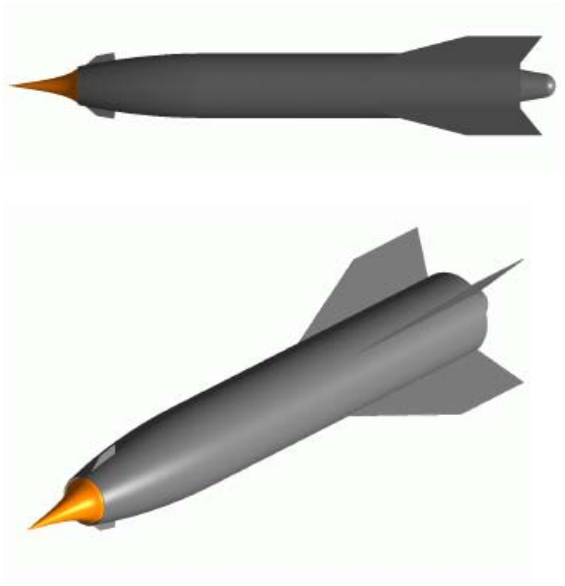

Figure 15: Artist's impression of SHyFE [7].

To keep development risk (and costs) low, a hydrocarbon fuelled annular ramjet combustor was proposed for the SHyFE vehicle. The design of the vehicle was such that it would fly at thermal equilibrium conditions during its cruise phase at Mach 6. Unfortunately, the program was canceled around the year 2008.

4.1 Kinematic Equilibrium Flight Conditions

The aerodynamic and propulsion modules of the Hypersonic Technology Evaluation Code (HyTEC) [8, 9] have been used to predict the integrated flight performance of the SHyFE vehicle. Figures 16 and 17 show some of the main aerodynamic characteristics as predicted by HyTEC over a flight Mach number range of 3 to 8 at altitudes ranging from 15 to 32 km.

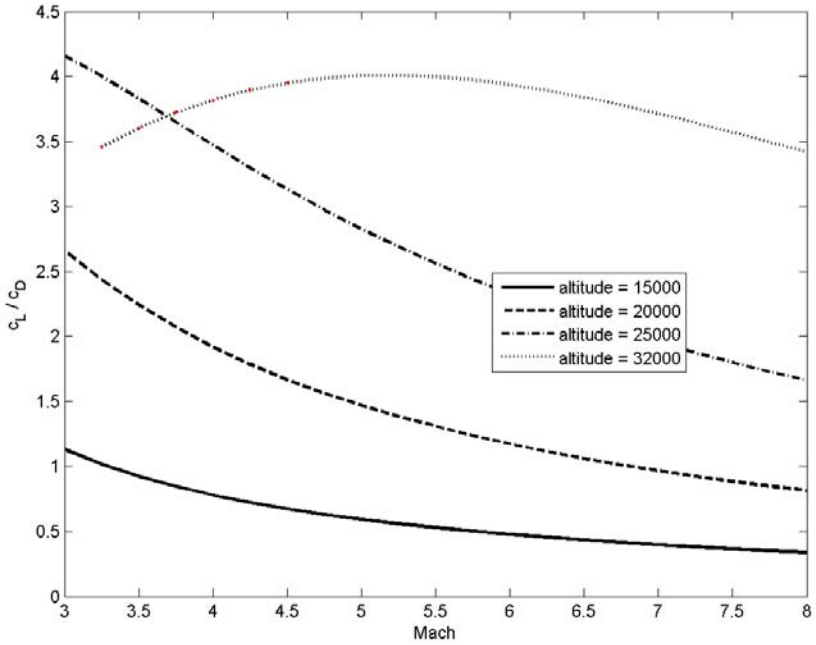

Figure 16: HyTEC predicted of the lift to drag ratio as a function of Mach number and altitude.

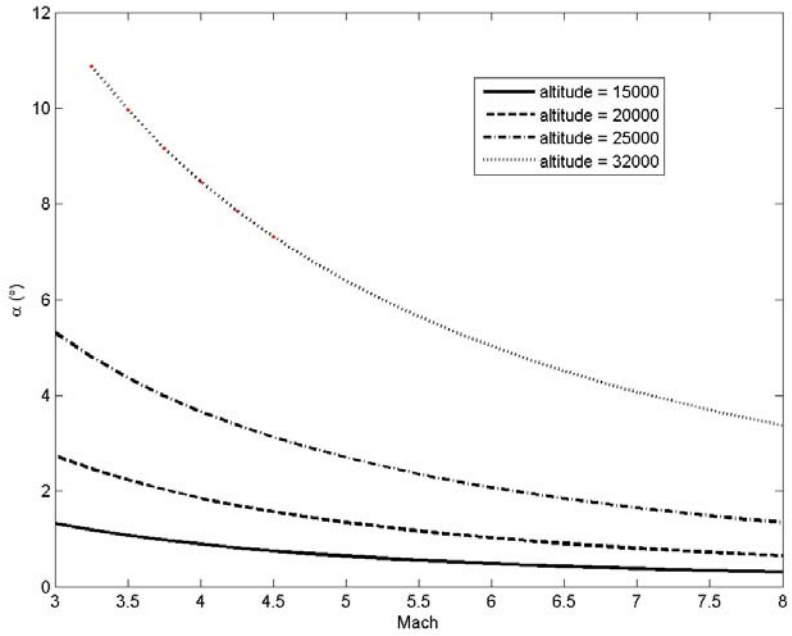

Figure 17: HyTEC predicted angle of attack a function of Mach number and altitude.

From Figure 16 it can be seen that the SHyFE vehicle's cruise Mach number of 6 is close to the Mach number at which optimum lift-to-drag ratio occurs at 32 km altitude. According to Figure 17 the predicted angle of attack at cruise flight conditions is about 5 degrees.

Figure 18 shows the specific impulse of the SHyFE propulsion system as predicted by HyTEC over a flight Mach number range of 3 to 8 at altitudes ranging from 15 to 32 km.

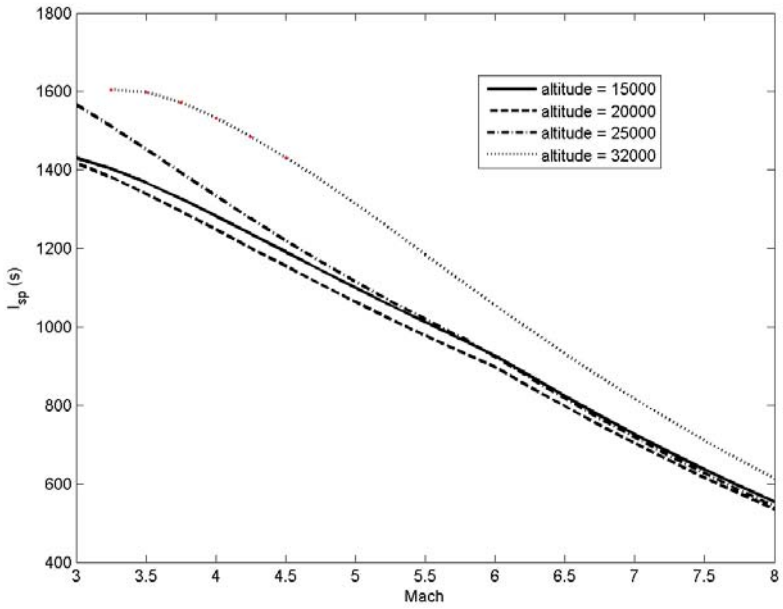

Figure 18: HyTEC predicted specific impulse as a function of Mach number and altitude.

The figure shows that the specific impulse decreases substantially when increasing the Mach number. This is due to the reducing propulsive efficiency of the subsonic combustion ramjet cycle at the high end of its operational envelope. At cruise flight conditions, a specific impulse around 1000 s is predicted by HyTEC.

Assuming a fuel mass fraction of 0.1, the predicted cruise range is shown in Figure 19. It can be seen that the SHyFE cruise flight conditions are very close to the predicted maximum flight range at 32 km altitude. The flight range at the cruise conditions of the SHyFE vehicle (Mach 6 at 32 km altitude) is predicted to be somewhat larger than 800 km. It should be noted here that all HyTEC calculation results assume the thrust to be equal to the drag. At the Mach number attitude combinations at which the SHyFE vehicle is accelerating, the HyTEC predictions do not represent the actual performance parameters in terms of fuel consumption, specific impulse, etc.

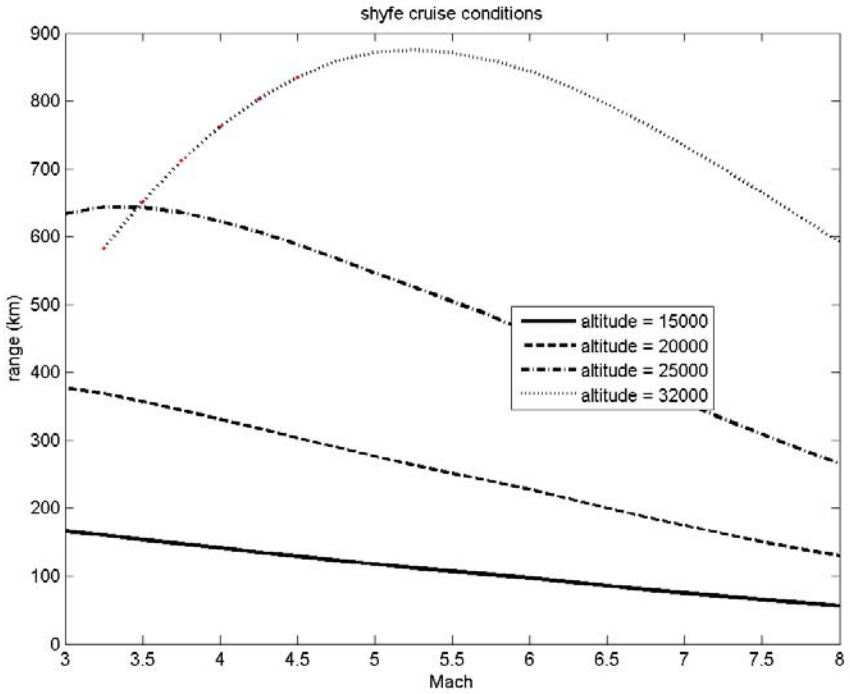

Figure 19: HyTEC predicted cruise flight range as a function of Mach number and altitude.

4.2 Thermal Equilibrium Conditions

The thermal model used to evaluate the thermal conditions of the SHyFE vehicle is depicted in Figure 20. As can be seen, the vehicle has a central body extending from the nose tip to the end of the plug nozzle. At the front end of the annular combustor the fuel (assumed to be Jet-A) is injected and instantaneous mixing and combustion is assumed. Combustion efficiency as well as dissociation effects are accounted for in the propulsion module of HyTEC and the thermal module uses the corresponding static gas temperature in the combustor for its thermal analysis.

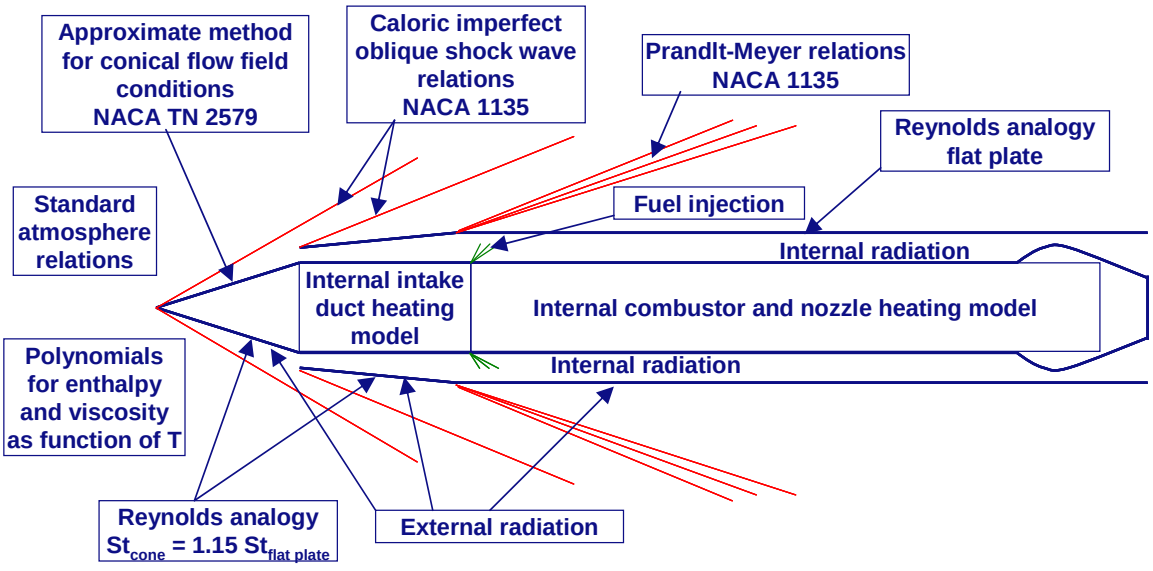

Figure 20: Thermal model description of the SHyFE vehicle.

All thermal model components as previously discussed are being used. External radiation is accounted for on all external surfaces assuming a value for the emissivity equal to 0.8. Internal radiation is accounted for using the equation for radiating concentric cylinders (Eq. (3.2)).

Figure 21 through 23 show the predicted equilibrium wall temperatures of the outer surface of the vehicle and of the wall of the centre body as a function of the x-coordinate along the vehicle for three different flight conditions. Also included are the adiabatic wall temperatures of the external and internal surfaces.

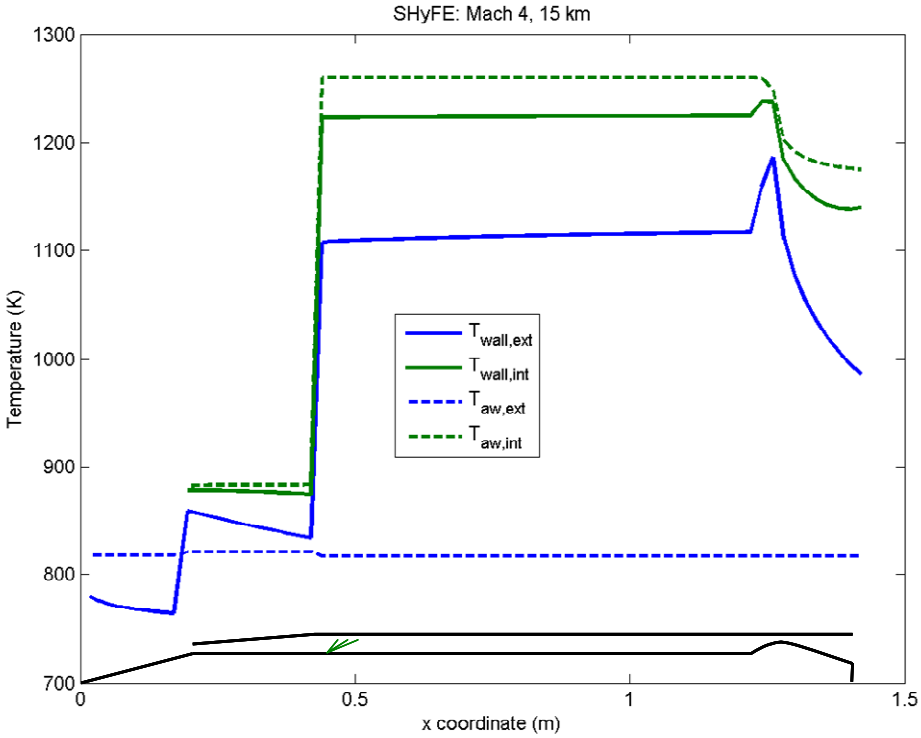

Figure 21: Predicted SHyFE vehicle external and internal wall temperatures at the Mach 4 and 15 km altitude.

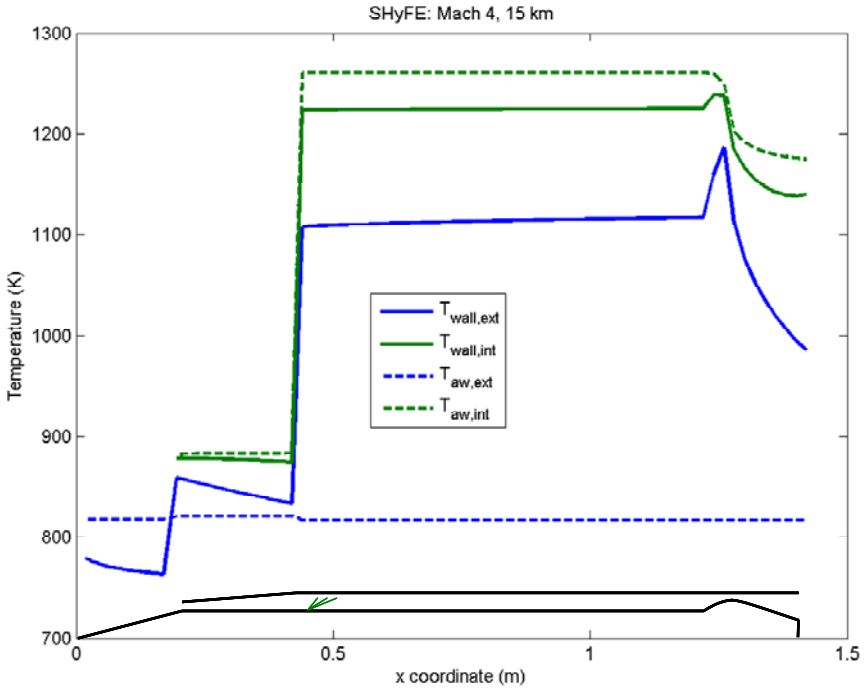

Figure 22: Predicted SHyFE vehicle external and internal wall temperatures at the Mach 5 and 20 km altitude.

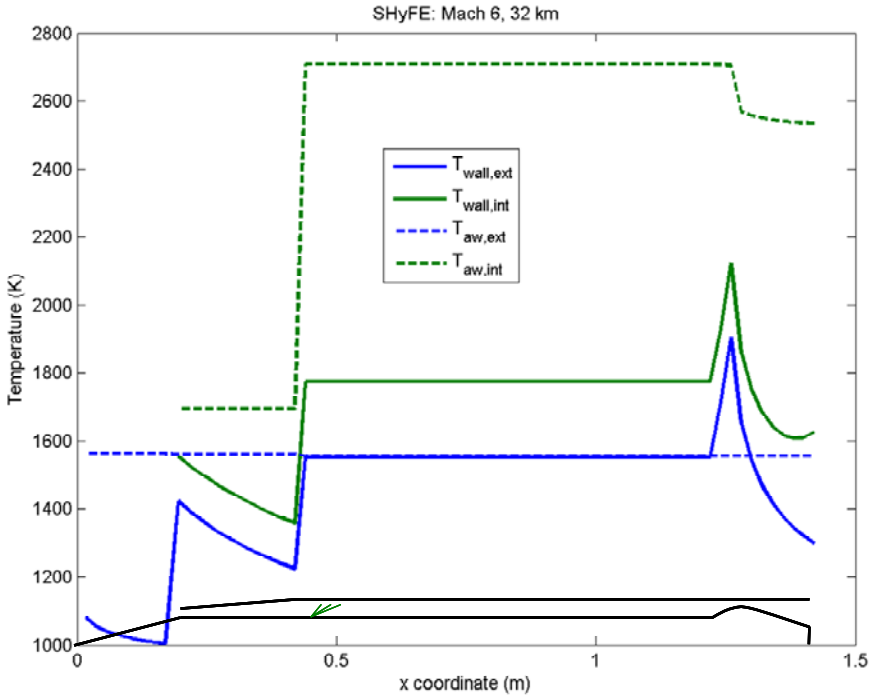

Figure 23: Predicted SHyFE vehicle external and internal wall temperatures at the Mach 6 and 32 km altitude.

The figures show a small step in external adiabatic wall temperature at the cowl-cylindrical body interface due to the local flow expansion. At the start of the combustion chamber a very steep rise in wall

temperature is visible as a result of the instantaneous mixing and combustion assumption. The heating of the external vehicle surface through radiation from the inner wall can be clearly seen; the external wall temperature at all flight conditions is significantly higher than the external adiabatic wall temperature. The highest wall temperatures are predicted for the highest flight speed; the inner combustor wall reaches a temperature of about 1750 K while the outer wall temperature is about 1550 K. At the nozzle throat, predicted peak wall temperature reach values of about 2100 K for the inner wall and 1900 K for the external vehicle wall. In the nozzle the wall temperatures quickly drop due the expansion process.

4.3 Angle of Attack Effects on Thermal Equilibrium Conditions

Figure 24 shows the predicted external and internal wall temperatures of the SHyFE vehicle at the windward and leeward body centre line for the Mach 6 at 32 km cruise flight condition taking into account the HyTEC predicted angle of attack of the vehicle. In the thermal model the intake nose cone angle and intake cowl angle were increased with the vehicle angle of attack at the windward side, while the angle of attack was subtracted from the nose cone and intake cowl angle at the leeward side. The expansion angle at the intake cowl interface to the cylindrical body was kept equal to the cowl deflection angle, resulting in the body wall to have a positive angle of attack at the windward side and a negative angle attack at the leeward side.

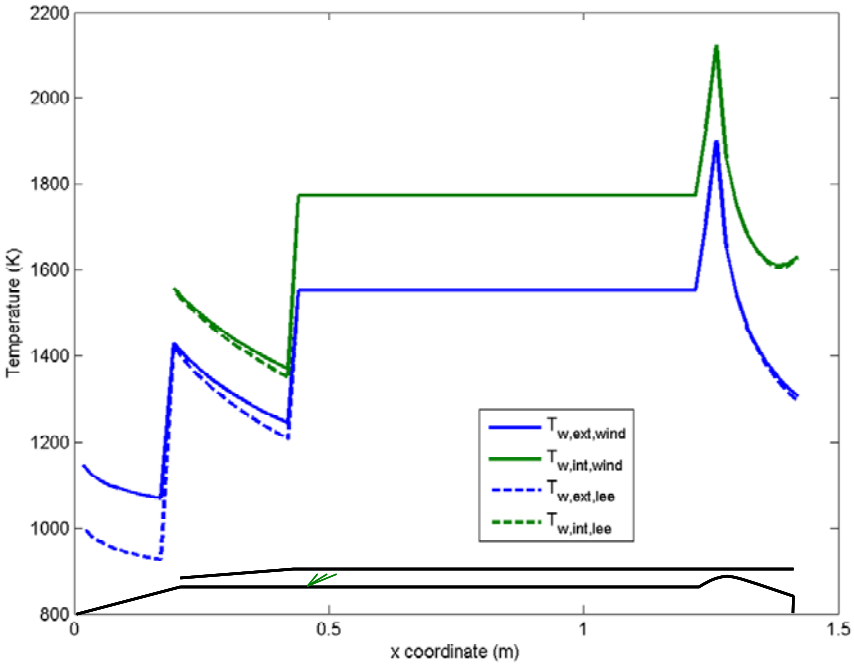

Figure 24: Predicted effect of the angle of attack on the SHyFE vehicle external and internal wall temperatures at the Mach 6 cruise condition at 32 km altitude.

As can be seen from Figure 24 all windward wall temperatures are equal to or higher than the temperatures on the leeward side of the vehicle. The angle of attack effect is visible most prominent on the intake nose cone. The effect of the approximately 5 degrees angle of attack is far less pronounced on the intake cowl. It can be seen, though, that the changed cowl wall temperature also affects the temperature of the inner wall of the internal intake duct. Hardly any effect is visible on the cylindrical body and combustor inner wall while at the aft end of the vehicle some minor effects show.

5.0 CONCLUDING REMARKS

Combining the thermal models described in the present lecture with the already existing HyTEC tool results in an integrated engineering system model capable of first order evaluations of the following aspects of a high speed airbreathing propelled vehicle:

- Aerodynamic performance.
- Propulsive performance.
- Thermal management.

The resulting integrated engineering tool allows for vehicle system level trade-offs in the early design stage of high speed airbreathing propelled vehicles.

The following aspects are considered for future extensions of the integrated engineering system tool:

- Include finite wall thickness.
- Include conduction (in axial and radial direction).
- Include a mixing and combustion ramp up zone in the combustor.
- Include radiation from combustion gasses.
- Include the option of multiple fuel injection locations.
- Conical flow field effects on the flare surface.
- Include vehicle acceleration capability (HyTEC).

6.0 ACKNOWLEDGEMENT

The author would like to thank his colleague Wouter Halswijk for his very efficient effort to translate the thermal model algorithms into a working MATLAB module of HyTEC. Without his help the lecture would have missed the interesting part on the application case of the SHyFE vehicle.

7.0 REFERENCES

[1] U.S. Standard Atmosphere, 1962, U.S. Government Printing Office, Washington, D.C., 1962.

[2] Ames Research Staff, ‘Equations, Tables, and Charts for Compressible Flow’, NACA Report 1135, Ames Aeronautical Laboratory, Moffett Field, California, 1953.

[3] S. Gordon and B.J. McBride, Computer Program for Calculation of Complex Chemical Equilibrium Compositions and Applications, NASA Reference Publication 1311, October 1994.

[4] A.J. Eggers Jr. and R.C. Savin, ‘Approximate Methods for Calculating the Flow about Nonlifting Bodies of Revolution at High Supersonic Airspeeds’, Ames Aeronautical Laboratory, Moffett Field, California, December 1951.

[5] L.F. Crabtree, R.L. Dommett and J.G. Woodley, ‘Estimation of Heat Transfer to Flat Plates, Cones and Blunt Bodies, R&M No. 3637, Ministry of Technology, Aeronautical Research Council, 1970.

[6] C.B. Rumsey and D.B. Lee, ‘Measurements of Aerodynamic Heat Transfer on a 15° Cone-Cylinder-Flare Configuration in Free Flight at Mach Numbers up to 4.7’, NASA TN D-824, Langley Research Center, Langley Field, Virginia, May 1961.

[7] T. Cain and C. Walton, 'The Sustained Hypersonic Flight Experiment', AIAA-2003-7030, 12th AIAA International Space Planes and Hypersonic Systems and Technologies, Norfolk, Virginia, Dec. 15-19, 2003.

[8] J.L.P.A. Moerel and W.H.C. Halswijk, 'System Analysis of High Speed, Long Range Weapon Systems', AIAA 2005-5819, AIAA Atmospheric Flight Mechanics Conference and Exhibit, San Francisco, 15-18 August 2005.

[9] J.L.P.A. Moerel and W.H.C. Halswijk, 'High Speed, Long Range Missiles – System Concepts and Integration', RTO-MP-AVT-135, RTO-AVT Innovative Missile Systems Symposium, Amsterdam, The Netherlands, May 15-19, 2006.